Bioactive Materials 40 (2024) 541–556

Contents lists available at ScienceDirect

Bioactive Materials

journal homepage: www.keaipublishing.com/en/journals/bioactive-materials

Engineering biomimetic silk fibroin hydrogel scaffolds with "organic-inorganic assembly" strategy for rapid bone regeneration

Renjie Liang [a,b,c,1], Rui Li [a,b,c,1], Weidong Mo [a,b,c,1], Xianzhu Zhang [a,b,c,e,1], Jinchun Ye [a,b,c], Chang Xie [a,b,c], Wenyue Li [a,b,c], Zhi Peng [a,b,c], Yuqing Gu [a,b,c], Yuxuan Huang [a,b,c], Shufang Zhang [a,b,c,d], Xiaozhao Wang [a,b,c,**], Hongwei Ouyang [a,b,c,d,*]

[a] Department of Sports Medicine of the Second Affiliated Hospital, and Liangzhu Laboratory, Zhejiang University School of Medicine, Hangzhou, China
[b] Dr. Li Dak Sum & Yip Yio Chin Center for Stem Cells and Regenerative Medicine, Zhejiang University School of Medicine, Hangzhou, China
[c] Zhejiang University-University of Edinburgh Institute, Zhejiang University School of Medicine, Haining, China
[d] China Orthopedic Regenerative Medicine Group (CORMed), Hangzhou, China
[e] Department of Orthopedics, The First Affiliated Hospital, Zhejiang University School of Medicine, 79 Qingchun Rd, Hangzhou, China

ARTICLE INFO

Keywords:
Silk fibroin
Organic-inorganic assembly
Mineralization
DLP 3D printing
Bone regeneration

ABSTRACT

Although natural polymers have been widely used in constructing bone scaffolds, it still remains challenging to fabricate natural polymer-derived bone scaffolds with biomimetic mechanical properties as well as outstanding osteogenic properties for large-size and weight-bearing bone defects regeneration. Herein, an "organic-inorganic assembly" strategy is developed to construct silk fibroin (SF)-based bone scaffolds with the aforementioned merits. After secondary structure reshuffling, the 3.3-fold increment of β-sheet structures in SF hydrogel resulted in a 100-fold improvement of mineral-assembly efficacy via influencing the ion adsorption process and providing templates for mineral growth. Notably, abundant minerals were deposited within the hydrogel and also on the surface, which indicated entire mineral-assembly, which ensured the biomimetic mechanical properties of the digital light processing 3D printed SF hydrogel scaffolds with haversian-mimicking structure. *In vitro* experiments proved that the assembly between the mineral and SF results in rapid adhesion and enhanced osteogenic differentiation of human bone marrow-derived mesenchymal stem cells. *In vivo* experiments further proved that the mineral-assembled SF hydrogel scaffold could significantly enhance integration and bone regeneration at the weight-bearing site within one month. This SF-based "organic-inorganic assembly" strategy sheds light on constructing cell-free, growth factor-free and natural polymer-derived bone scaffolds with biomimetic 3D structure, mechanical properties and excellent osteogenic properties.

1. Introduction

The Bone defect, especially at weight-bearing sites, caused by tumor resection and severe trauma has become a challenging clinical problem and severely compromises the life quality of patients [1,2]. Utilizing bone scaffolds with 3D structures is a promising strategy for better integration and restoring bone function [3]. Commercially available bone prostheses are mostly made from titanium alloy and polyether-ether-ketone [4–6]. Although the aforementioned prostheses possess outstanding mechanical properties to restore motor function and provide mechanical support, they barely degrade and exist as foreign implants to the host, which may lead to the activation of inflammatory

Peer review under responsibility of KeAi Communications Co., Ltd.
* Corresponding author. Center for Stem Cells and Regenerative Medicine, Zhejiang University School of Medicine, No.866 Yuhangtang Road, Xihu District, Hangzhou, 310058, China.
** Corresponding author. Center for Stem Cells and Regenerative Medicine, Zhejiang University School of Medicine, No.866 Yuhangtang Road, Xihu District, Hangzhou, 310058, China.
E-mail addresses: 11818043@zju.edu.cn (R. Liang), ruili@intl.zju.edu.cn (R. Li), 3200103266@zju.edu.cn (W. Mo), 11518129@zju.edu.cn (X. Zhang), 21918382@zju.edu.cn (J. Ye), xiechang@zju.edu.cn (C. Xie), wenyueli@zju.edu.cn (W. Li), 21918137@zju.edu.cn (Z. Peng), 11918137@zju.edu.cn (Y. Gu), 12118614@zju.edu.cn (Y. Huang), zhangshufang@zju.edu.cn (S. Zhang), xiaozhaowang@zju.edu.cn (X. Wang), hwoy@zju.edu.cn (H. Ouyang).
[1] These authors contributed equally to this research.

https://doi.org/10.1016/j.bioactmat.2024.06.024
Received 24 February 2024; Received in revised form 15 June 2024; Accepted 15 June 2024

reactions [7–9]. Thus, commercial prostheses seldom realize complete regeneration of large-size and weight-bearing bone defects; besides, they might threaten the host's health in the long run. To address these problems, biodegradable natural polymers with remarkable biocompatibility are adopted for bone scaffold construction.

As natural bone extracellular matrix (ECM) is mainly an assembly of protein polymer (mainly collagen) and hydroxyapatites (HAps), collagen-based or collagen-derived materials, such as acellular matrix, animal tissue-derived collagen and gelatin are widely used in bone tissue engineering to mimic bone ECM [10,11]. With a deeper understanding of the natural bone mineralization mechanism, polymer-induced amorphous calcium phosphate (ACP) is gradually used to penetrate collagen fibers for intrafibrillar hydroxyapatite assembly, which further makes collagen-derived scaffolds more chemically biomimetic and possess enhanced osteogenic properties [12]. Nevertheless, the collagen-dependency of the ACP-based strategy might hinder its application in large-size and weight-bearing bone regeneration [13]. Currently, commercial collagen mainly derives from animal tissues, which means high costs and virus transmission risks. Besides, 3D structure is favorable for the integration between the scaffold and host tissue [14,15]; however, the feasibility of constructing collagen-derived scaffolds with customized 3D structure and large size simultaneously is usually doubted. Taken together, a new strategy is urgently needed to construct protein polymer-derived bone scaffolds with biomimetic mechanical and excellent osteogenic properties as well as elaborate 3D structures for large-size and load-bearing bone defects.

Silk fibroin (SF) is another kind of natural protein polymer. Specifically, SF from *Bombyx mori* has been widely used in biomedical research due to its outstanding biocompatibility and large-scale production [16]. Besides, it has been approved by Food and Drug Administration (FDA) for used in medical devices, which means SF-derived scaffolds have great potential for clinical uses [17]. Recent studies also identified that SF could be chemically modified for digital light processing (DLP) 3D printing [18]. With the help of DLP 3D printing, it is much easier to obtain customized and biomimetic 3D structures for matching the defect's shape and promoting scaffold-host tissue integration. It has also been demonstrated that the compressive modulus of SF-derived scaffolds can range widely from kilopascal to gigapascal by using different processing methods and modulating the secondary structure of SF [19–21]. For instance, when treated with low-polarity reagents, such as ethanol and methanol, the β-sheet content of SF could be significantly increased, which also enhances the mechanical properties [22]. Moreover, many researchers found that the existence of β-sheet structure is beneficial for HAps growth [23–26]. SF hydrogel is a water-containing 3D network. Thus, it is speculated that by modulating SF's secondary structure, the DLP 3D printed SF hydrogel scaffold with abundant β-sheets could be assembled with HAps both inside and outside to finally get the SF-derived bone scaffold with biomimetic mechanical properties and 3D structure.

Further, the early microenvironment shaped by implanted scaffolds within the defect plays a pivotal role in enhancing bone regeneration efficiency [27]. These scaffolds offer a spectrum of chemical, physical, and biological factors that intricately interact with cells involved in the regeneration process, collectively modulating the microenvironment. SF, renowned for its exceptional processability and mechanical properties, emerges as a natural biomaterial that fosters beneficial interactions with cells, fostering an immune microenvironment conducive to tissue regeneration [28,29]. Similarly, hydroxyapatite nanoparticles (HAps), widely utilized in bone tissue engineering, exhibit an ability to engage with mesenchymal cells, fostering an environment favorable for bone regeneration [30]. Moreover, the mechanical cues provided by these scaffolds significantly influence the microenvironment. Biomimetic scaffolds, mimicking the mechanical properties of native tissue, have demonstrated efficacy in promoting tissue regeneration [31]. Thus, in this study, geared towards clinical application, we aim to develop a cell-free and growth factor-free bone scaffold inducing a favorable *in situ* microenvironment for efficient bone regeneration.

Herein, we report an integrated strategy to prepare SF-derived bone scaffolds with biomimetic mechanical properties, 3D structure and excellent osteogenic properties for highly efficient regeneration of large-size and weight-bearing bone defects (Scheme 1). The chemical modification enables SF to be processed by DLP 3D printing to construct hydrogel scaffolds with customized and biomimetic 3D structure. Reshuffling the secondary structure of SF influences the ion adsorption and provides templates for mineral growth, leading to remarkably increased mineral-assembly efficiency of SF hydrogel. Therefore, the DLP printed 3D scaffold could be well assembled with HAps with our strategy and the compressive modulus of the scaffolds could be increased by 60 times to 2.33 MPa, which suggests chemically and physically biomimetic. The *In vitro* experiments prove that the assembly of the organic phase (SF hydrogel) and the inorganic phase (HAps) remarkably enhances the adhesion and osteogenic differentiation of human bone marrow-derived mesenchymal stem cells (hBMSCs). The *In vivo* study further proves that the assembled SF hydrogel scaffold could significantly prevent the deformation of bone defects at the load-bearing site; it also ensures highly efficient integration and bone regeneration by inducing a favorable microenvironment at the early stage.

2. Results

2.1. β-sheet structure promotes the assembly of HAps in silk fibroin hydrogel

According to our previous work, the SF was modified by glycidyl methacrylate (GMA) to get methacrylated SF (SilMA), which could crosslink to form SF hydrogel with 405 nm light and photo-initiator, lithium phenyl-2,4,6-trimethylbenzoylphosphinate (LAP) [29]. As it has been proved that the existence of β-sheets is beneficial to biomineralization, we expected that SF hydrogel with more β-sheets could be better mineralized when immersed in simulated body fluid (SBF). Thus, ethanol was adopted to increase the β-sheet proportion in SilMA-derived hydrogel (Silgel). After being treated with ethanol, a 3.3-fold increment of β-sheet crystallites was realized (Fig. 1A and B; Fig. S1). To investigate whether the increment of β-sheet crystallites would mediate the mineralization of Silgel, ethanol-treated Silgel (E) and non-treated Silgel (Control) were immersed in 1.5 × SBF under human body temperature (37 °C) and sectioned at designed time intervals for characterization (Fig. 1C). The transmission electron microscopy (TEM) images revealed that the increment of β-sheet crystallites promotes the growth of minerals inside Silgel (Fig. 1D). Energy dispersive spectrometer (EDS) elemental mapping results indicated that the minerals contained abundant Ca and P elements (Fig. 1E). The high-resolution TEM (HR-TEM) images, selected area electron diffraction (SAED) patterns and X-ray diffraction (XRD) further confirmed that the minerals were HAps and grew better with more β-sheet crystallites in SF (Fig. 1F & Fig. S2). Thus, the *in vitro* study proved initially that the increment of β-sheet crystallites could promote the growth of HAPs inside Silgel. Unlike precedingly reported results that increased β-sheet crystallites only lead to surface mineral coating of materials [24–26], our results illustrated that increased β-sheet crystallites could lead to internal mineralization of Silgel.

To further verify our *in vitro* findings, ethanol-treated Silgel (E) and non-treated Silgel (Control) were implanted subcutaneously in rats to verify the *in vitro* results (Fig. 2A). After 4 weeks of implantation, the samples were harvested and characterized. Micro-computed tomography (Micro-CT) scanning results reveal that Silgel with significantly increased β-sheet crystallites displayed areas with an augmented signal while the control group did not (Fig. 2B and C). Masson trichrome staining results demonstrated that red-staining areas only existed in E samples; the shapes of those areas also matched the parts with the augmented signal in micro-CT images (Fig. 2D). Observed by scanning electron microscopy (SEM), the red-staining areas (also the signal-

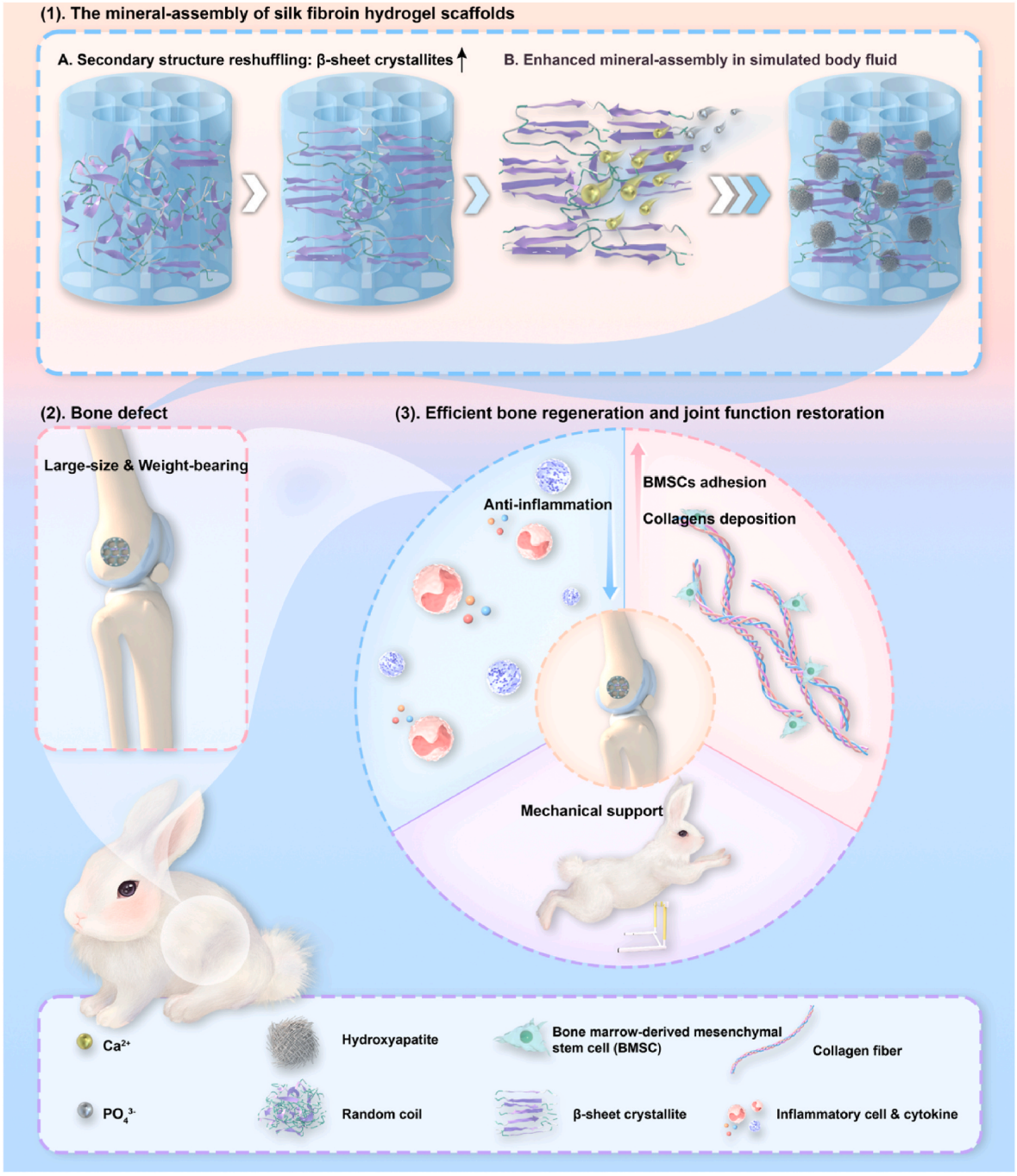

Scheme 1. Schematic illustration of constructing mineral-assembled silk fibroin hydrogel scaffolds with biomimetic 3D structure, suitable mechanical properties and excellent osteogenic properties for rapid bone regeneration.

augmented areas in micro-CT images) displayed graininess morphology while the blue-staining areas had a smooth appearance (Fig. 2E). EDS elemental mapping results proved that the substance with graininess morphology contains abundant Ca and P elementss; besides, the Ca/P ratio is close to 1.67, indicating the minerals are HAps (Fig. 2F–H). Therefore, after secondary structure reshuffling by ethanol, the increment of β-sheet crystallites in E resulted in subcutaneous mineralization, which is consistent with the *in vitro* results (Fig. 1). Taken together, the ethanol-induced conformational reshuffling leads to a significantly increased proportion of β-sheet crystallites which further promotes the mineral-assembly of Silgel both *in vitro* and *in vivo*.

2.2. The "organic-inorganic assembly" increases 47-fold compressive modulus of haversian-bone-mimicking Silgel scaffolds

It has been proved that the biomimetic structure of scaffolds could promote scaffold-host integration and bone regeneration [3]. The photo-crosslinking merit of SilMA ensures that it can be processed with DLP 3D printing technology to obtain Silgel scaffolds with bone-mimicking structures and designed sizes. Thus, a haversian-mimicking 3D model (diameter: 8 mm, height: 6 mm; diameter for the inner canals: 2 mm) was designed first and Silgel scaffolds with designed 3D structure and size were obtained (Fig. 3A and B). The Silgel scaffolds (SGS) were divided into three groups. The first group remained untreated (SGS). The samples of the second group were only

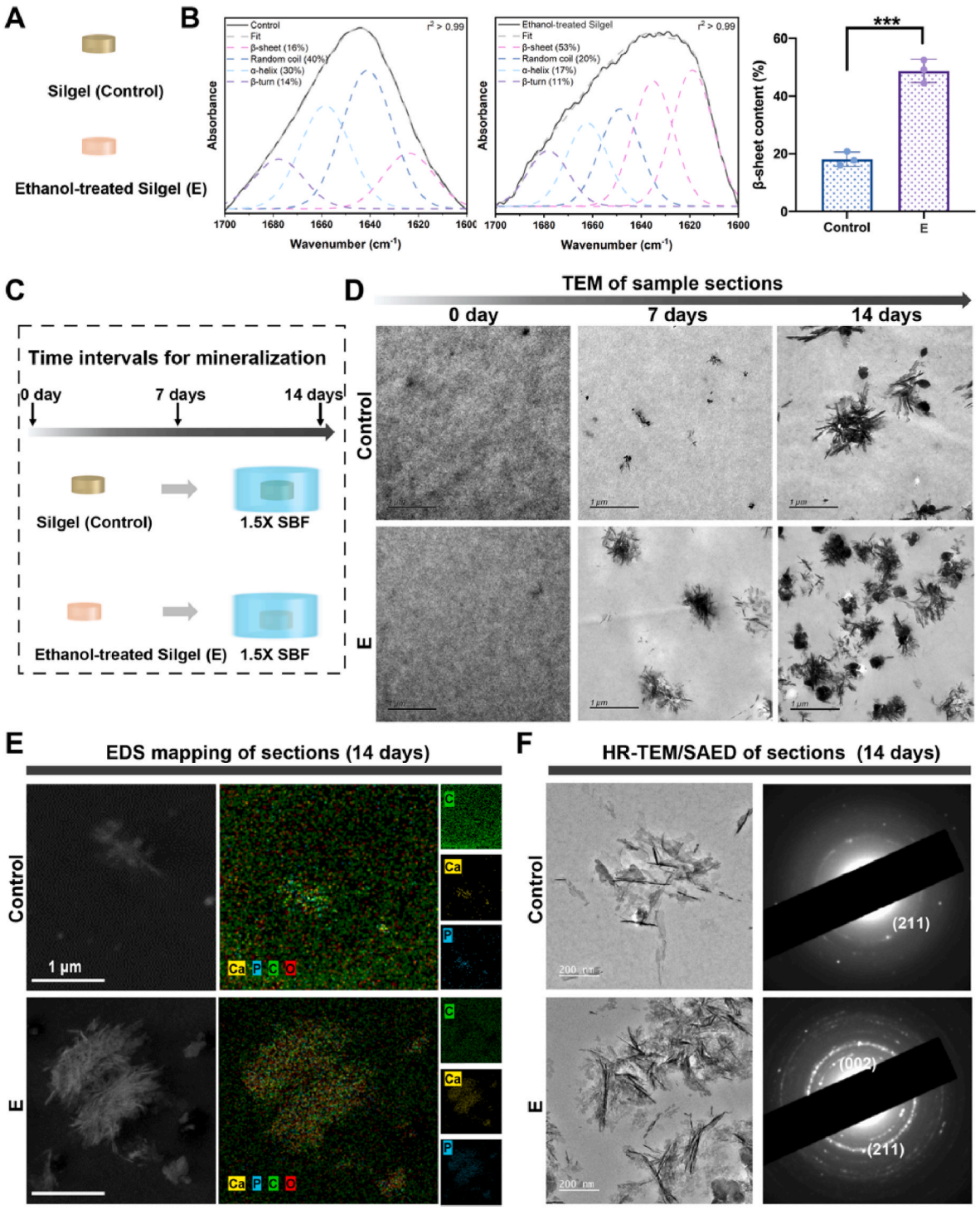

Fig. 1. β-sheet crystallites promote the mineral-assembly of Silgel *in vitro*. A) Schematic for the processing method of increasing β-sheet content. B) FTIR spectra of the untreated Silgel (control) and the ethanol-treated Silgel (E); quantitative analysis of secondary structures. All data are presented as mean ± SD, (n = 3), ***p < 0.001. C) Schematic for the mineralization process. D) TEM images of sample sections at different time points. E) EDS elemental mapping images, F) HR-TEM images and SAED images of the mineral crystallites inside the Silgel after 14 days of mineralization.

reshuffled by ethanol to increase the β-sheet crystallite content and named ES. The samples of the third group (EMS) were treated according to the aforementioned "organic-inorganic assembly" strategy which means reshuffling the secondary structure first, and then being immersed in 1.5 × SBF for 4 weeks. To characterize the inner morphology and elemental compositions, all kinds of scaffolds were sectioned and characterized with SEM/EDS mapping. According to the SEM images, the SGS displayed a porous structure, while the ES and EMS were compact (Fig. 3C). Further EDS elemental mapping revealed that hydroxyapatites existed in EMS (Fig. 3C–E). For the bone defect with large-size and at the weight-bearing site, the mechanical properties of the haversian-mimicking scaffolds are also crucial. Therefore, the mechanical properties of the scaffolds were tested to verify whether they were qualified. The EMS group had a rupture strain of approximately 73 %, which was significantly higher than that of SGS (35 %) and E groups (55 %) (Fig. 3F, Fig. S3). Amazingly, the strength of EMS group (3.67

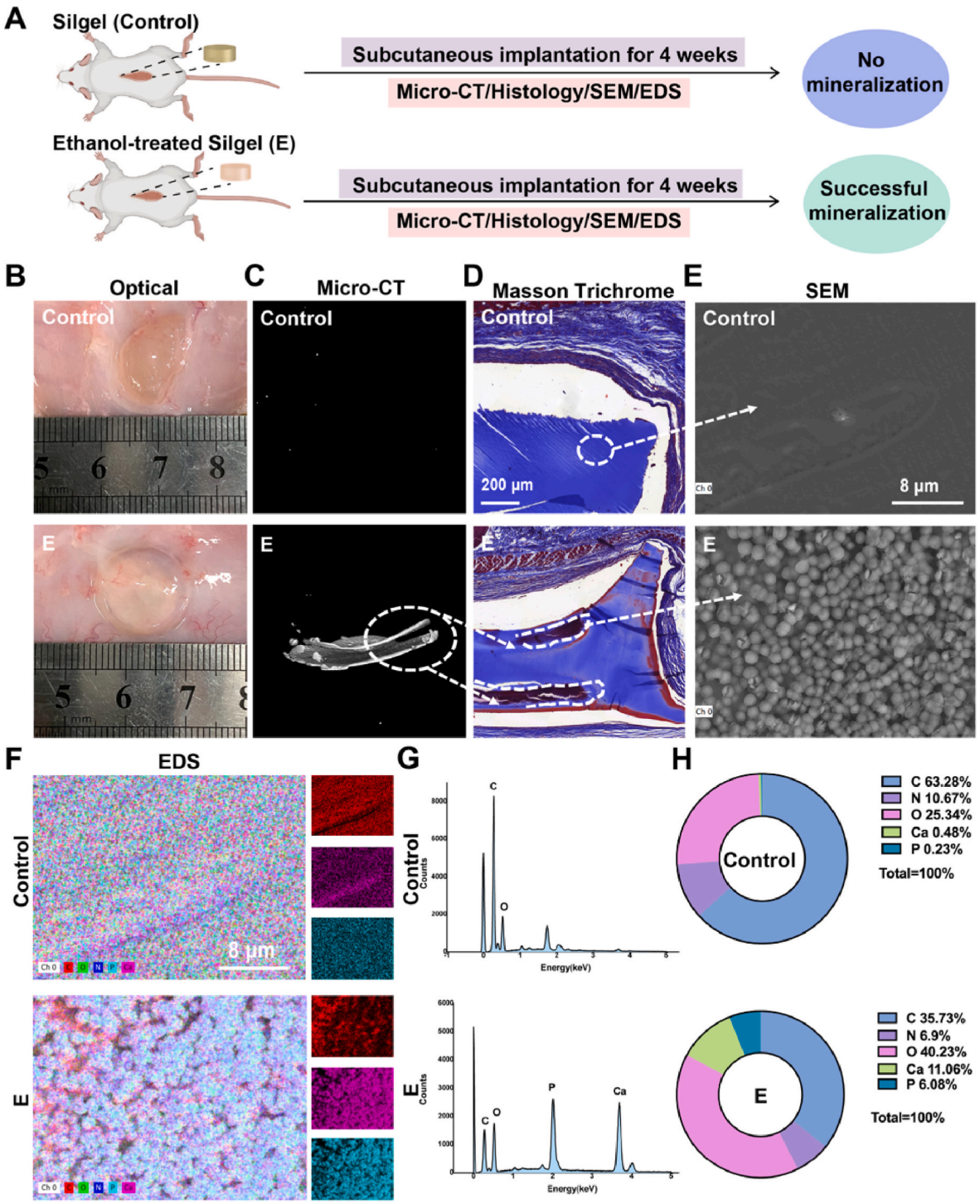

Fig. 2. β-sheet crystallites promote the mineral-assembly of Silgel *in vivo*. A) Schematic for the subcutaneous mineralization experiments. B) Gross pictures and C) micro-CT images of the harvested samples. D) Masson trichrome images of the sample sections. E) SEM images, and F, G) EDS elemental mapping results of the selected sample areas, indicated by white dashed line frames in D). H) Atoms proportion, derived by the EDS elemental mapping results.

MPa) was 200 times higher than that of the SGS group (Fig. 3F, Fig. S3). The compressive modulus of EMS group (2.33 ± 0.18 MPa) was also remarkably higher than that of ES (0.49 ± 0.05 MPa) and SGS (0.05 ± 0.02 MPa) (Fig. 3G, Fig. S3). Therefore, the compressive modulus of the Silgel-derived scaffold was augmented by around 46.6 times after mineral-assembly and also within the range of compressive modulus of human cancellous bone (between 0.145 and 13.535 MPa) [32]. Together, combining DLP 3D printing platform and the "organic-inorganic assembly" strategy, the Silgel-derived scaffold with haversian-liking structure and biomimetic mechanical properties could be successfully constructed.

2.3. *The secondary structure conformation of the Silgel influences the ion-adsorption process*

To figure out how the secondary structure conformation of the Silgel affects the assembly process, Silgel was loaded on Mo mesh firstly and photo-crosslinked consequently. For the E group, the samples were

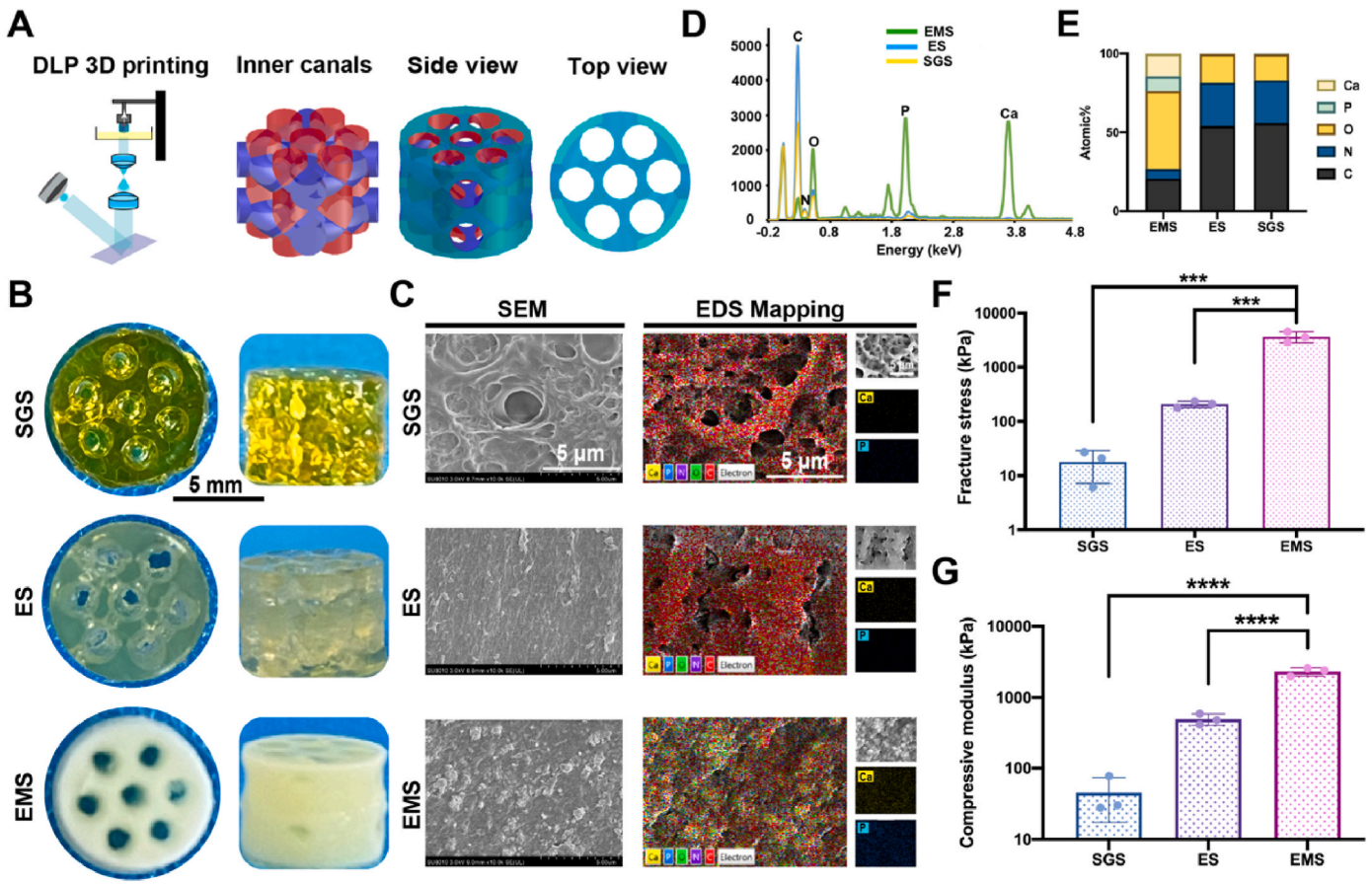

Fig. 3. The "organic-inorganic assembly" strategy enhances the mechanical properties of haversian bone-mimicking Silgel scaffolds. A) Schematic diagram of DLP 3D printing system and the haversian-mimicking 3D model. B) Gross view of different Silgel-derived scaffolds; Silgel scaffold (SGS), ethanol-treated Silgel scaffold (ES), ethanol-treated first and then mineralized Silgel scaffold (EMS). C) SEM characterization of the morphology and EDS analysis of element composition of different Silgel-derived scaffold sections. D) The characteristic peaks of EDS spectra for elements. D) The percentage of the main elements in different scaffolds. F) Strength of different Silgel-derived scaffolds. G) Compressive modulus of different Silgel-derived scaffolds. All data are presented as mean ± SD, (n = 3), ***p < 0.001, ****p < 0.0001.

immersed in Ethanol for conformational reshuffling, washed by ddH_2O and finally floated on the surface of 1.5 × SBF; for the control group, the samples were directly floated on the surface of 1.5 × SBF (Fig. 4A). TEM images illustrated that after conformational reshuffling, there were dark granules in both groups; however, the density of the dark granules was much higher in samples of the E group which possesses more β-sheet crystallites (Fig. 4B). To further quantify the density of the dark granules, samples at day 5 were observed with cryo-TEM. According to the reconstruction of the 3D tomography results, it was confirmed that the dark granules were mainly inside the Silgel for both E and control groups (Fig. 4C). After that the volume ratio of the inside dark mineral granules to the Silgel was calculated, it turned out that the density of the dark granules was 100 times higher in samples of the E group (with 3.3-fold increment of β-sheet crystallites) than that of the control group samples (Fig. 4C). Hence, substantially more mineral granules could be deposited in the reshuffled Silgel (E) samples within the same period. To investigate how the dark mineral granules formed in the Silgel, TEM (80 kV) and EDS elemental mapping experiments were conducted. Firstly, with the scanning transmission electron microscopy mode, it was further verified that the mineral granules were mostly inside the Silgel samples for both E and control groups (Fig. 5A). The EDS elemental analysis results at different time intervals revealed that with more β-sheet crystallites, the Silgel samples (E group) adsorbed more Ca which exists as Ca^{2+} in 1.5 × SBF, and consequently adsorbed more P which exists as PO_4^{3-} in 1.5 × SBF (Fig. 5A). Amino acids information and zeta potential results revealed that conformational reshuffling barely changed the negative charge of Silgel (Fig. S4). Based on the above results, it was suggested that after the ethanol-induced conformational reshuffling, the significantly increased β-sheet crystallites favored the interaction with Ca^{2+}, making the Silgel more positively charged and inducing the following adsorption of PO_4^{3-}, which then led to the mineral-assembly of the Silgel (Fig. 5B). Previous research proved that the mineralization process is dictated by the electronegative amino acids in the amorphous fractions [33]. In this study, we reshuffled the secondary structure of the Silgel using ethanol to increase the β-sheet crystallite content by 3.3 folds. The reshuffled secondary structure could enhance the ion adsorption process and β-sheet crystallites could act as templates for mineral growth, together leading to superior mineral-assembly.

2.4. *The mineral-assembled Silgel promotes hBMSCs adhesion and osteogenic differentiation*

Next, the osteogenic ability of the mineral-assembled Silgel was examined. BMSCs play a crucial role in bone regeneration, which can undergo osteogenic differentiation to promote bone regeneration [34,35]. Therefore, we investigated the effect of the mineral-assembled Silgel on hBMSCs to evaluate its osteogenic properties. Firstly, three different forms of Silgels were prepared: untreated Silgel group (Control), ethanol-treated Silgel (with abundant β-sheet crystallites) group (E), and both ethanol-treated and mineral-assembled Silgel group (EM). hBMSCs were seeded on all three forms of Silgels. After 24 h of cell culture, hBMSCs maintained high viability (>90 %) on all three kinds of

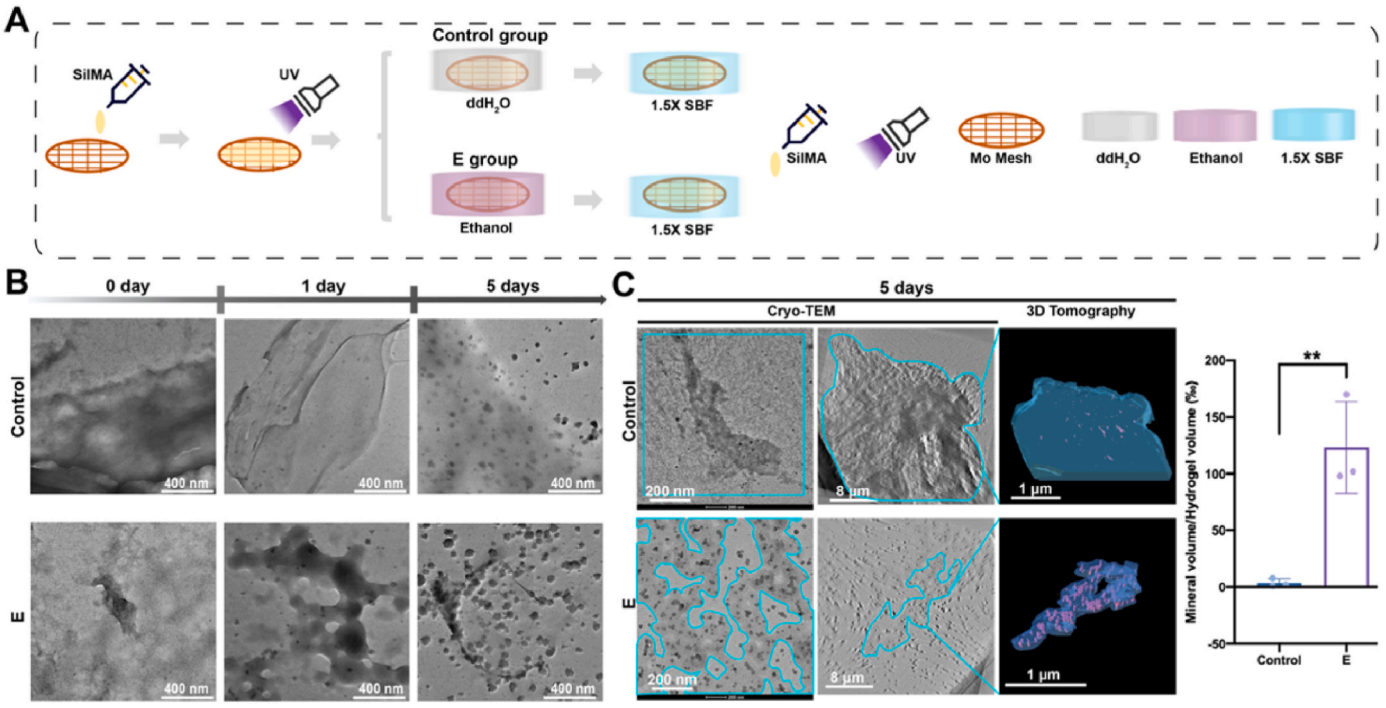

Fig. 4. The increment of β-sheet crystallites promotes the deposition of mineral granules inside Silgel. A) Schematic for the Mo mesh-based *in vitro* experiments. B) TEM images of samples at different time points. C) Cryo-TEM images, reconstruction images of 3D tomography and the quantification result. The closed blue frames in the first column indicate the shape of the Silgel. The blue closed frames in the second column indicate the area for 3D tomography analysis. All data are presented as mean ± SD, (n = 3), **p < 0.01.

Silgels (Fig. 6A and B), indicating no cytotoxicity for all materials. The cell density at 24 h was also quantified, it turned out that the β-sheet crystallite enrichment in the E group led to a decrease in the number of adhered hBMSCs compared with control hydrogels (Fig. 6C). Notably, the mineral assembly after the β-sheet crystallite enrichment significantly increased the density of adhered hBMSCs (Fig. 6C), which suggested that the mineral-assembly promoted the adhering of hBSMCs. SEM images revealed that hBMSCs on the E samples displayed a more sparse and elongated shape than those on the control samples (Fig. 6D). On the EM samples, hBMSCs exhibited a polygonal shape similar to hBMSCs on control hydrogels but with significantly higher cell density (Fig. 6D). Overall, ethanol treatment brings more β-sheet crystallites and hydrophobic regions, leading to a declined adhesion rate of hBMSCs. Fortunately, further mineral assembly of E hydrogel (EM) restores rapid adhesion of hBMSCs with significantly higher density.

In addition, the effects of various forms of Silgels on the osteogenic differentiation of hBMSCs were evaluated. The hBMSCs were seeded on the surface of three different forms of Silgels and then underwent osteogenic differentiation with an osteogenic differentiation medium for 7 days. As presented in Fig. 6E, the alkaline phosphatase (ALP) staining results showed that the E and EM samples exhibited more pronounced coloration than the Control group. Quantitative analysis demonstrated a 2-fold ALP activity increment in the E and EM groups (Fig. 6F). However, there was no significant difference between Group E and Group EM. In addition, quantitative real-time polymerase chain reaction (qPCR) was carried out to detect osteogenic differentiation-related genes at the transcriptional level after 7 days of osteogenic induction. The expression of osteogenic genes including ALP, osteocalcin (OCN), collagen type I (COL-1), and runt-related transcription factor 2 (RUNX2) was significantly upregulated in the EM group compared with the Control and E groups (Fig. 6G). The Control and E groups showed no significant difference in the expression level of osteogenic differentiation-related genes. Further, Alizarin Red S (ARS) staining was further performed to evaluate the late-stage osteogenic potential of the scaffolds. According to the ARS staining results, EM samples showed the strongest osteogenic ability (Fig. S5). These results together demonstrate the high osteogenic capacity of EM hydrogels, prepared with our "organic-inorganic assembly" strategy. Taken together, our "organic-inorganic assembly" strategy could be utilized and combined with DLP 3D printing to construct natural polymer-derived scaffolds with biomimetic 3D structure, mechanical properties and excellent osteogenic properties for *in vivo* applications.

2.5. The mineral-assembled Silgel scaffold facilitates highly efficient regeneration of large-size bone defects at weight-bearing sites

To further evaluate the *in vivo* therapeutic efficiency of our strategy, cylinder-shaped defects were established in the lateral condyle of New Zealand White rabbits' distal femurs which have a weight-bearing function. The cylinder-shaped defect had a height of 6 mm and a diameter of 8 mm, which was relatively large for rabbits. As presented in Fig. 3, three forms of Silgel scaffolds were prepared including Silgel scaffold (SGS), ethanol-treated Silgel scaffold (ES) and mineral-assembled ES (EMS). All Silgel-derived scaffolds possessed haversian-like structure and matched the size of the defects (Fig. 3A and B). Autologous cancellous bone (ACB) transplantation is widely used to treat large-size bone defects; therefore, ACB was used as a positive control group. Besides, the non-treated defect was considered as a negative control group. Thus, the defects were then treated in four ways, including non-treatment for the Blank group, and implanted with SGS, ES, EMS, and ACB respectively (Fig. 7A). After implantation, the 3D printing scaffolds matched well with the defect site (Fig. S6A). After 4 weeks, the femur bones of the Blank, SGS, ES and ACB groups showed some degree of deformation, while the bones in the EMS group maintained the normal shape (Figs. S6B and C). Besides, the defect was covered well by regenerated smooth tissue in EMS group, while the defect surface in the ES group lacked tissue coverage and there were significant fibrous scars in the Blank and SGS groups (Fig. S6B). Together, it is concluded that EMS can provide sufficient mechanical support at the weight-bearing site to prevent bone deformation and

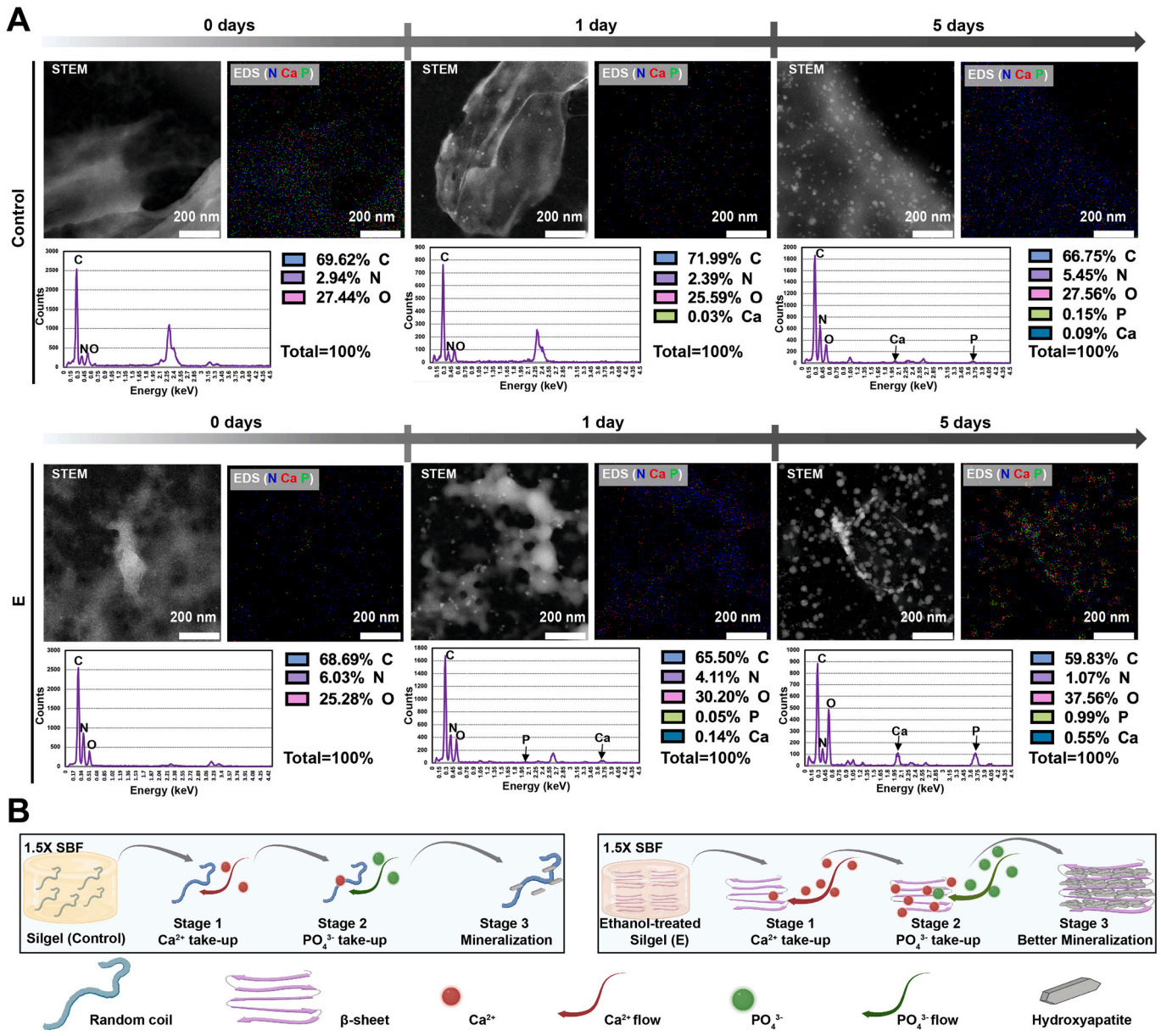

Fig. 5. The increment of β-sheet crystallites influences the ion-adsorption process in Silgel. A) STEM images, EDS elemental mapping images, characteristic peaks of EDS spectra for main elements and the percentage of main elements. B) Schematic diagram for the organic-inorganic assembly process for Silgels without/with secondary structure reshuffling.

promote tissue regeneration.

Furthermore, micro-CT analysis was used to reveal the bone regeneration status 4 weeks postoperatively. The 3D reconstruction images showed no obvious new bone formation in the Blank group, SGS group, and ES group, whereas significantly enhanced bone regeneration was found in the EMS group characterized by more calcification and hard tissue formation in the defects (Fig. 7B). Besides, new bone tissue was clearly observed growing into the canals of EMS. The 3D reconstruction images of the ACB group showed that the filled autologous cancellous bone was still present in the defect region (Fig. 7B). Quantitative morphometric analysis of the micro-CT results also confirmed that the EMS group and ACB group had significantly higher bone volume fractions (bone volume/tissue volume, BV/TV), 48.15 ± 12.68 % and 51.78 ± 9.734 % respectively, than the other three groups (Blank: 8.833 ± 4.645 %, SGS: 10.83 ± 8.106 %, ES: 10.33 ± 8.106 %), (Fig. 7C). The EMS group and ACB group also had significantly higher bone mineral density (BMD) values, 1429 ± 343 g/cm3 and 1623 ± 212.9 g/cm3 respectively, than other groups (Blank: 463.2 ± 166.6 g/cm3, SGS: 468.1 ± 294.4 g/cm3, ES: 410.4 ± 192.4 g/cm3) (Fig. 7D). Therefore, the EMS significantly promoted weight-bearing bone regeneration within 4 weeks.

Subsequently, hematoxylin and eosin (H&E) staining and Masson trichrome staining of the regenerated bone were performed and the representative images were shown in Fig. 7E, **F**. According to the H&E staining images, the Blank group displayed abnormal bone resorption with the defect changing from cylindrical to irregular shape with no significant new bone formation in the defect area (Fig. 7E). Residual Silgels were still present in the defect region of the SGS group, and there was no obvious new bone tissue in the defect area (Fig. 7E). There were many areas without tissue in-growth of the ES group samples, indicating poor integration with *in situ* host tissue (Fig. 7E). In contrast, a significant amount of new bone growth was observed in the scaffolds of the EMS group (Fig. 7E). The defect of the ACB group was filled with disordered autologous cancellous bone fragments (Fig. 7E). Similarly,

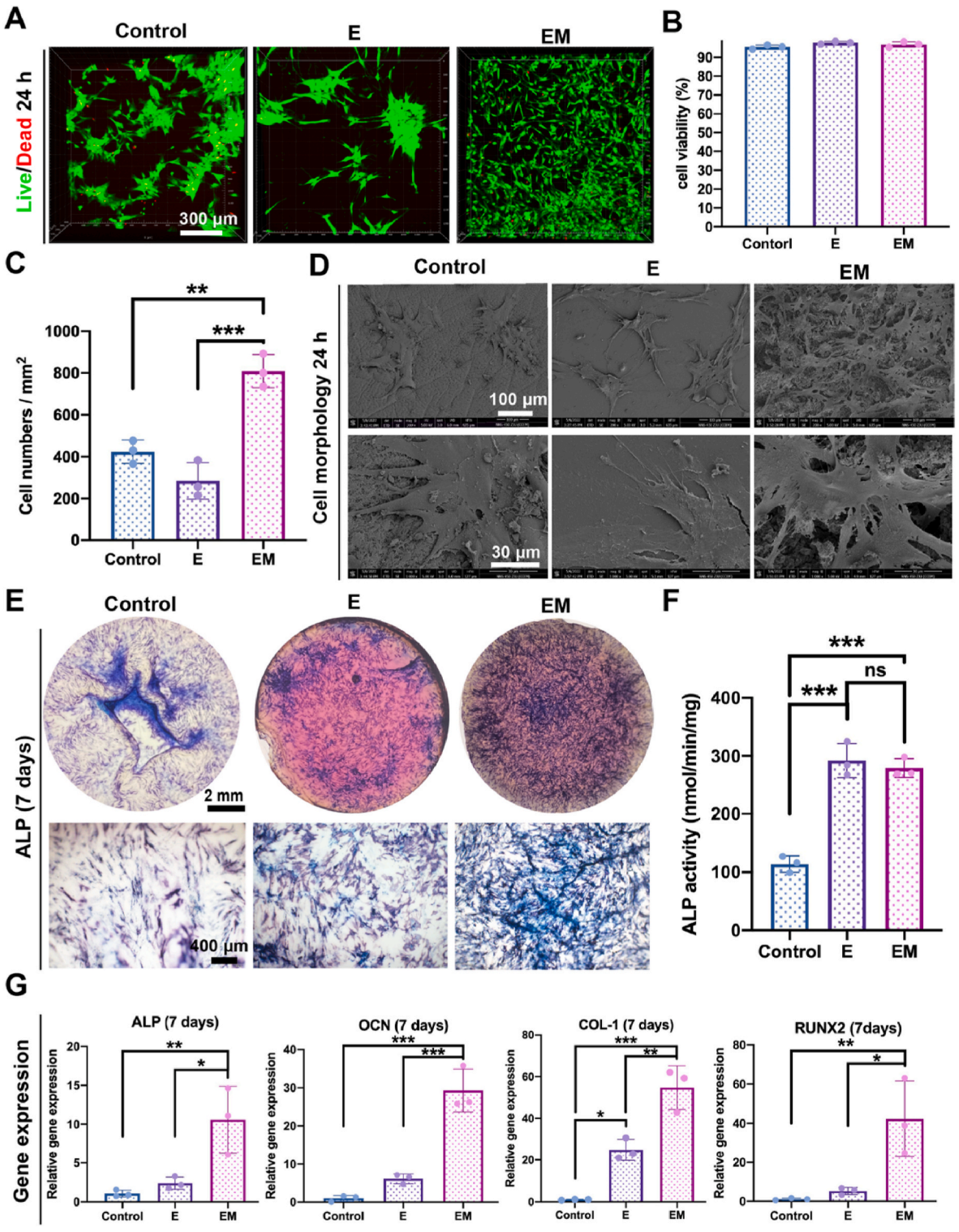

Fig. 6. Mineral-assembled Silgel promotes the adhesion and osteogenic differentiation of hBMSCs. A) Live/dead staining for hBMSCs seeded on the surface of different forms of Silgel for 24 h. Untreated Silgel (Control), ethanol-treated Silgel (E), ethanol-treated and mineral-assembled Silgel (EM). B) Quantitative results of cell viability. C) Quantitative results of cell density. D) SEM images of cell morphology. E) ALP staining images and F) quantification of ALP activity after 7 days of osteogenic differentiation. G) Relative expression of osteogenic differentiation-related genes. All data are presented as mean ± SD, (n = 3), *p < 0.05, **p < 0.01, ***p < 0.001.

the results of Masson trichrome staining confirmed a large amount of new bone formation in the EMS group, comparable to the ACB group, whereas bone ingrowth was barely observed in the Blank, E, and ES groups (Fig. 7F). Therefore, the histological staining results demonstrated that the EMS can promote bone regeneration and integrate well with host tissue within 4 weeks. The high-efficiency regeneration and integration could also be partially explained by the *in vitro* experiment results that the mineral-assembled Silgel is capable of promoting hBMSCs adhesion and osteogenic differentiation.

As the postoperative microenvironment at the defect is crucial to the

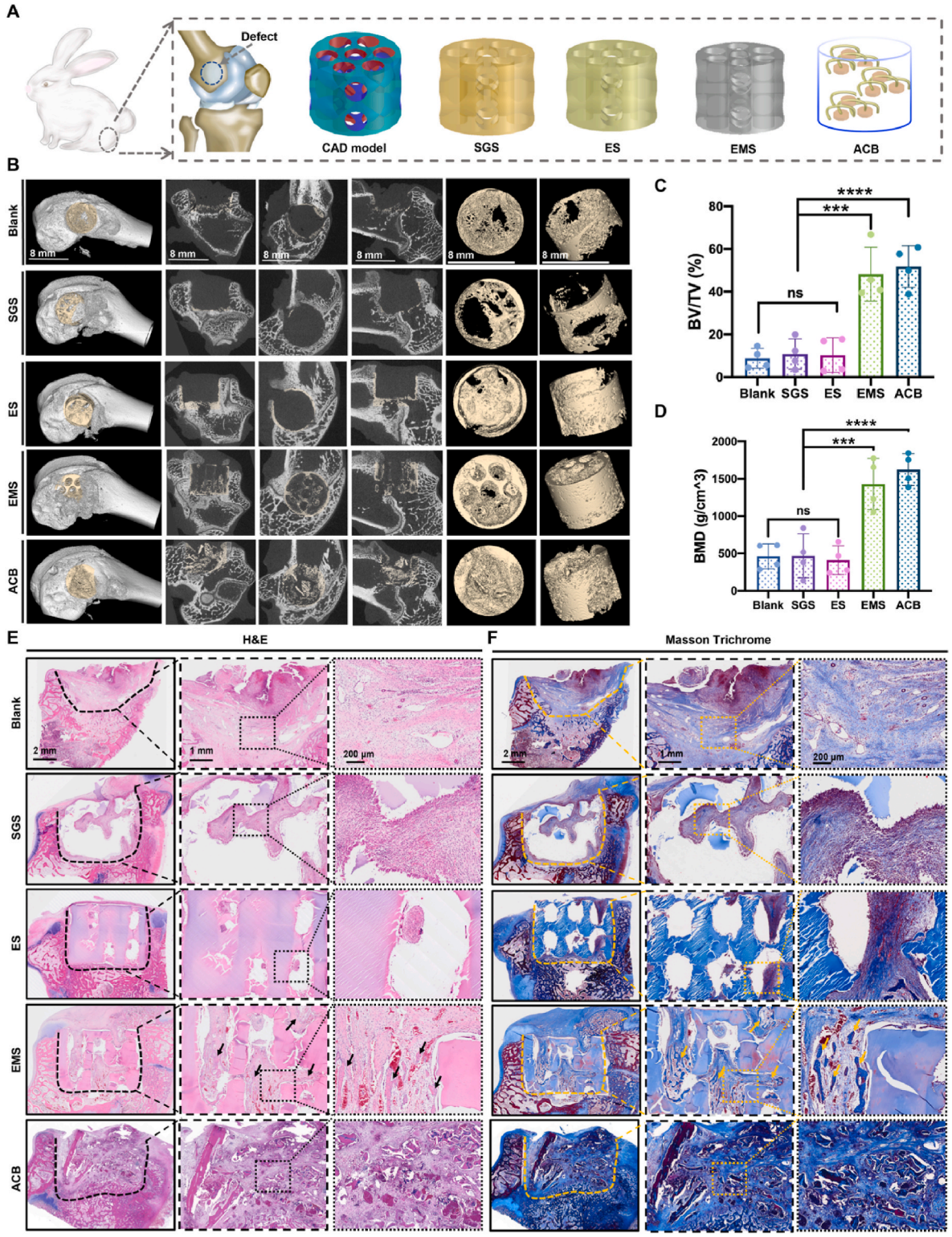

Fig. 7. EMS facilitates the regeneration of large-size and weight-bearing bone defects. A) Schematic diagram of the modeling location (lateral condyle of the distal femur) in New Zealand White rabbits and different treatments. B) 3D reconstructed micro-CT scanning images of bone defects and regenerated bone tissue induced by different treatments, with yellow cylinders indicating the defect location. C, D) Quantitative morphometric analysis of the bone volume fraction (bone volume/tissue volume, BV/TV) and bone mineral density (BMD) of the newly formed bone analyzed with micro-CT scanning. E) Representative H&E staining images of differently treated groups after 4 weeks postoperatively, with black arrows indicating new bone. F) Representative Masson trichrome staining images of differently treated groups after 4 weeks of repair, with yellow arrows indicating new bone. All data are presented as mean ± SD, (n = 4), ***p < 0.001, ****p < 0.0001, ns: not significant.

healing outcomes [27,36,37], transcriptome sequencing was further performed to investigate how the EMS modulates the *in situ* microenvironment to achieve high-efficiency bone regeneration (Fig. S7A). From the principle component analysis (PCA) diagram, it was evident that the gene sets of the EMS group and the other groups exhibited clear clustering, and that the samples were highly repeatable (Fig. S7B). Volcano plot images visualized the differentially expressed genes ($Q < 0.05$, $|\log2\text{-Fold}| > 1$) between the EMS group and other groups (Figs. S7C–E). Based on the Gene Ontology (GO) database, the enrichment of biological processes of differentially expressed genes in EMS group compared with other groups was analyzed. The results of GO analysis showed that compared with the Blank group, the differentially expressed genes down-regulated in the EMS group were mainly enriched in the cellular response to hypoxia, intrinsic apoptosis signaling pathway, antibacterial humoral immune response mediated by antimicrobial peptides, neutrophil aggregation and chemotaxis, while the differentially expressed genes up-regulated in the EMS group were mainly enriched in biological processes such as bone development, ossification and chondrocyte development involved in endochondral bone morphogenesis (Fig. 8A). Compared with the SGS group, the differentially expressed genes down-regulated in EMS group were mainly enriched in leukocyte tethering or rolling, while the significantly up-regulated genes in the EMS group were mainly enriched in apoptotic cell clearance (Fig. 8B). Compared to the ES group, the differentially

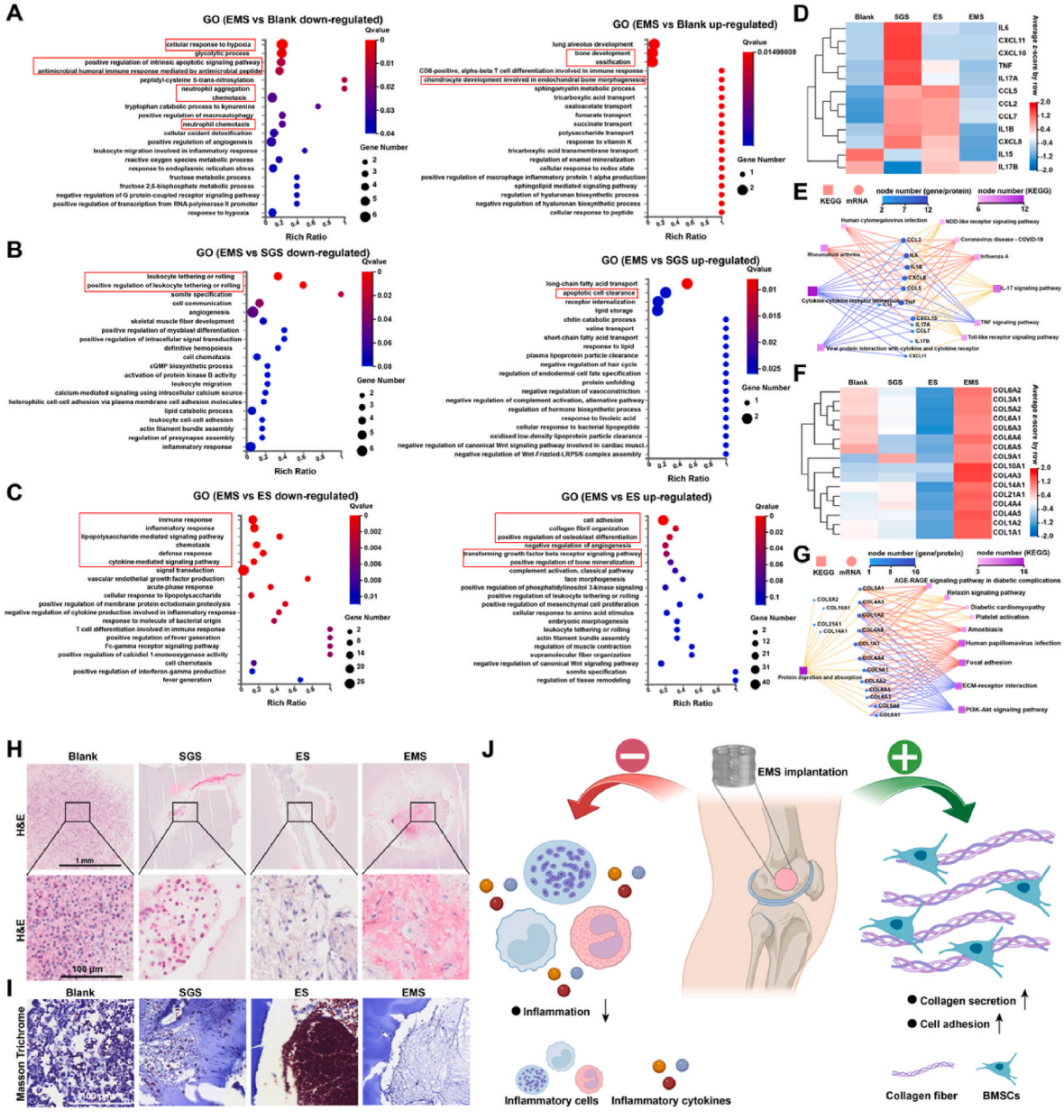

Fig. 8. Transcriptome sequencing demonstrates a favorable microenvironment for high-efficiency bone regeneration induced by EMS. A-C) GO enrichment analysis of differentially expressed genes ($Q < 0.05$ is considered as significantly enriched). D) The heatmap of the differentially expressed genes involved in inflammation. Cutoff: $Q < 0.05$, $|\log2\text{-Fold}| > 1$. E) The KEGG Pathway network diagram of genes involved in inflammation. The square represents the KEGG Pathway, and the circle represents mRNA. Both color and size represent the number of genes or transcripts connected to the node. The darker the color and the larger the square, the more genes or transcripts are connected to the node. Different color lines represent different classifications of Pathway, red for cellular processes, blue for environmental information processing and yellow for organic systems. F) The heatmap of the differentially expressed and collagen-encoding genes. Cutoff: $Q < 0.05$, $|\log2\text{-Fold}| > 1$. G) The KEGG Pathway network diagram of collagen-encoding. H) Representative H&E staining images of the sequenced tissue. I) Representative Masson trichrome staining images of the sequenced tissue. J) Schematic for the microenvironment induced by EMS.

expressed genes down-regulated in the EMS group were still primarily enriched in biological processes associated with inflammation, whereas the differentially expressed genes up-regulated in the EMS group were primarily enriched in biological processes associated with cell adhesion, collagen fibril organization, and bone regeneration (Fig. 8C). Collectively, it can be concluded that EMS can inhibit inflammation, stimulate collagen secretion, and promote cell adhesion.

To further validate our findings, inflammation-related genes and collagen-related genes were further analyzed. Firstly, the expression levels and the Kyoto Encyclopedia of Genes and Genomes (KEGG) pathway networks were analyzed for genes involved in inflammatory response (inflammatory cytokine genes: IL1B, IL6, IL17A, IL17B, IL15 and TNF; chemokine genes: CCL2, CCL5, CCL7, CXCL8, CXCL10 and CXCL11) and genes involved in collagen secretion, such as COL1A1, COL1A2, COL6A1, COL6A2 and COL10A1 (Fig. 8D–G). The heatmap images and the KEGG pathway network analysis results together verified our findings that using EMS could induce a low-inflammation microenvironment with abundant collagen secretion and deposition shortly after operation. H&E and Masson trichrome staining of the sequenced tissues were also performed, the representative images illustrated mild immune cell infiltration and abundant collagen deposition in samples of the EMS group, whereas immune cell aggregation and few collagen fibers were observed in other groups (Blank, ES and EMS) (Fig. 8H and I). Therefore, the EMS-form scaffold could induce a favorable *in situ* microenvironment featuring low inflammation and abundant collagen deposition to realize high-efficiency bone regeneration (Fig. 8J). In summary, the enhanced mechanical properties and microenvironment-modulating capacities of the mineral-assembled EMS scaffold facilitate the high-quality regeneration of large-sized and load-bearing bone defects.

3. Discussion

The regeneration of large-size and weight-bearing bone defects presents a significant challenge in modern medicine. Commercially available bone prostheses, typically composed of materials like titanium alloy and polyether-ether-ketone, have been successful in restoring motor function and providing necessary mechanical properties. However, these prostheses, being foreign to the host, carry the potential risk of complications and long-term threats to distal organs [38,39]. In contrast, natural biomaterials offer superior biocompatibility and biodegradability, but their use in constructing bone grafts with biomimetic mechanical properties, biomimetic 3D structures, and potent osteogenic abilities has remained a formidable task. Natural bone's extracellular matrix (ECM) primarily comprises organic (protein) and inorganic (hydroxyapatite) components. Inspired by this substance assembly of natural bone ECM, we explored an integrated strategy to fabricate biomimetic bone grafts.

Many pioneer researches proved that β-sheet crystallites can act as templates for minerals to grow [24,25,40–43]. Inspired by those findings, in this study, a significant enrichment of β-sheet crystallites within a silk fibroin-derived hydrogel (Silgel) was induced by ethanol to promote mineralization. Surprisingly, a 3.3-fold increment of β-sheet crystallites led to a remarkable 100-fold increase in the efficiency of mineral granules deposition inside the silk fibroin hydrogel when immersed in simulated body fluid (SBF) (Fig. 4). Unlike previously reported results that β-sheet crystallites typically promote the formation of minerals on the surface of SF-based or SF-containing materials [24,25,40–43], the mineral granules observed in this study were both inside the hydrogels (Figs. 1–3)and on the surface (Figs. 3 and 6), which indicated fully mineral-assembled Silgel. This organic-inorganic assembly significantly enhanced the compressive modulus of the 3D-printed haversian-like scaffold by 46.6 times (from 0.05 MPa to 2.33 MPa). This compressive modulus is roughly aligned with that of human cancellous bone, which typically ranges from 0.145 to 13.535 MPa [32]. By combining DLP 3D printing with our "organic-inorganic assembly" strategy, we can construct Silgel-derived bone grafts that possess biomimetic 3D structure and mechanical properties, suitable for clinical applications.

To further validate the therapeutic efficacy of our mineral-assembled bone grafts. Both *in vitro* and *in vivo* experiments were conducted. The mineral-assembled Silgel displayed excellent properties in promoting the adhesion and osteogenic differentiation of human bone marrow-derived mesenchymal stem cells (hBMSCs) (Fig. 6). *In vivo* results demonstrated that the DLP 3D-printed and mineral-assembled scaffold (EMS), facilitated efficient and deformation-resistant bone regeneration. On one hand, due to its precisely controlled 3D structure, it integrated seamlessly with the defects and provided channels for fast cell infiltrating (Figure S6 and Fig. 8H). On the other hand, the scaffolds (EMS) chemically and physically mimicked natural cancellus bone, proving biomimetic material substances and mechanical properties, which resulted in a favorable microenvironment for efficient bone regeneration at the early stage (Fig. 8). The microenvironment was characterized by low inflammation and abundant collagen deposition. Specifically, hBMSCs cultured on the mineral-assembled Silgel displayed a significantly higher expression level of collagen (Fig. 6G), consistent with the *in vivo* results (Fig. 8H), indicating that EMS interacted positively with cells involved in bone regeneration. However, further studies are still needed to reveal the underlying mechanisms of how those chemical and physical cues interact with cells, leading to the pro-regenerative microenvironment for bone regeneration. Inspired by Zhang's research [28], multi-omics techniques could be utilized in our future study to figure out the regulatory pathways, accounting for the microenvironment-modulating capacity of the mineral-assembled grafts.

While our study illustrates the positive effect of increased β-sheet crystallites on the efficiency of the mineral-assembly process and demonstrates the mechanical as well as biological function changes, future work is still needed to deeply investigate the mineralization mechanism for precise modulation. A previous study proved that the electronegative amino acids (containing carboxyl group) in the amorphous fraction of SF dictate the mineralization process [33]. Besides, it is also proved that β-sheet crystallites act as templates for minerals to grow leading to better mineralization on the material surface [24,25,40–43]. According to our results, after secondary structure reshuffling, there was only a subtle change in the electric charge of the Silgel (Fig. S5), while it was more likely to adsorb Ca^{2+} at the very beginning and displayed significantly enhanced mineralization efficiency (Fig. 5). Thus, we rationally speculate that after the formation of more β-sheet crystallites, the electronegative chemical groups like carboxyl group, in the amorphous region of SF, are more exposed to interact with Ca^{2+} and the presence of abundant β-sheet crystallites also favors the growth of HAps, leading to mineral-assembly of the Silgel. To understand the whole process more accurately, a molecular dynamics simulation model will be utilized by our team to visualize the molecular mechanism in future studies.

Moreover, the mineral-assembly efficiency increases with the content of β-sheet crystallites, which necessitates the quantitative study about how the content/proportion of β-sheet crystallites influences the mineral-assembly efficiency. By deciphering the quantitative relationship between the content of β-sheet crystallites and mineral-assembly efficiency, scientists could precisely control the mineral-assembly degree to meet requirements for different bones or for different individuals. Further, combined with the 3D printing technology and secondary structure reshuffling methods, scaffolds with spatially heterogenous β-sheet crystallite contents could be fabricated, which means spatial control over the mineralization degree. Additionally, another concern of the application of natural polymer-derived bone graft is the fixation method. In clinical practice, doctors confront different shapes of bone defects at different locations. Most of the cases are highly dependent on internal fixation. Nevertheless, it is still challenging to internally fix natural polymer-derived bone grafts, compared with metal-based or synthetic polymer-based grafts. Thus, the fixation issue should be addressed for natural polymer-derived bone grafts.

Overall, our findings highlight the significance of manipulating the secondary structure of Silgel to control the mineral-assembly efficiency of the scaffold. Combining these findings with the remarkable processability of silk fibroin, this study pioneered an "organic-inorganic assembly' strategy to create single-polymer silk fibroin-derived bone scaffolds. These scaffolds exhibited customized 3D structures, biomimetic mechanical properties, and exceptional osteogenic capabilities. The assembled scaffold (EMS) has shown promising therapeutic efficacy in regenerating large-size and weight-bearing bone defects. Thus, our work introduces an integrated and practical strategy for constructing cell-free, growth factor-free, structured, and functionalized natural protein polymer-derived grafts, potentially serving as suitable alternatives to autologous and allogeneic bone grafts, and offering new avenues for bone tissue engineering.

4. Conclusion

In summary, we have successfully constructed natural polymer (silk fibroin)-derived bone grafts with biomimetic 3D structure, mechanical properties and excellent osteogenic properties, using DLP 3D printing and our "organic-inorganic assembly" strategy. The mineral-assembled scaffolds are superior in promoting hBMSCs adhering and osteogenic differentiating *in vitro*. *In vivo,* experiments further substantiate the capacity of the mineral-assembled scaffolds in realizing high-efficiency bone regeneration via inducing a favorable microenvironment, characterized by low inflammation and abundant collagen deposition at the early stage. Consequently, this study unveils a promising strategy to construct natural polymer-derived biomimetic bone grafts for large-size and weight-bearing bone regeneration.

5. Materials and methods

5.1. FTIR spectroscopy to detect the secondary structure of different forms of Silgels

Two forms of Silgels were prepared. Briefly speaking, Silgels were prepared from glycidyl methacrylate (GMA)-modified SF. According to our previous work, SF (ZHEJIANG XINGYUE BIOTECHNOLOGY CO., LTD) was modified by GMA (Sigma Aldrich) to get methacrylated SF (SilMA), which could crosslink to form Silgel with 405 nm light and photo-initiator, lithium phenyl-2,4,6-trimethylbenzoylphosphinate (LAP) [29]. Firstly, SilMA was dissolved using ddH_2O to obtain its 30 % (wt/v) solution, containing 1 % (wt/v) LAP. For the control group, the solution was only crosslinked by UV light to obtain Silgel cylinders (diameter = 10 mm, height = 5 mm); for the ethanol group, the Silgel cylinders were further treated with ethanol for 24 h. The samples were freeze-dried and then ground into powder. Fourier-transform infrared spectroscopy (FT-IR, Vertex 70, Bruker, Germany) was used to collect the FT-IR spectra of Silgel samples (650 - 4000 cm^{-1}) with 32 wavelength scans at a resolution of 4.0 cm^{-1}. After subtracting the baseline, the amide I (about 1600–1700 cm^{-1}) was analyzed by the second derivatization and further Gaussian curve fitting via PeakFit v4.12 software. The wavenumber of individual component peaks indicated different secondary structures of Silgels.

5.2. X-ray diffraction (XRD) to detect the secondary structure of different forms of Silgels

The presence of β-sheet crystals in different groups of Silgel powders were detected by an X-ray diffractometer (Bruker, D8 ADVANCE) with a scanning speed of 0.2 s/step.

5.3. XRD to characterize different forms of Silgels

Three forms of Silgels were prepared, (Non-treated Silgel (Control), Ethanol-treated Silgel (E), and Mineralized ethanol-treated Silgel (EM)). For the control and E cylinder samples, they were prepared according to section 5.1. For the EM samples, the E cylinders were immersed in 1.5 × simulated body fluid (SBF) (Solarbio®) under human body temperature (37 °C) for 14 days. All samples were freeze-dried and ground into powder. All sample powders were analyzed using an X-ray diffractometer (Bruker, D8 ADVANCE) with a scanning speed of 0.2 s/step.

5.4. TEM to characterize mineralization of different forms of Silgels

Mineralization of molybdenum mesh loaded samples: the 5 % (wt/v) SilMA precursor solution was filtered through a 0.22 μm Millex-GP filter, and 20 μL of the diluted solution was added dropwise onto a 100-mesh ultra-thin elastomeric molybdenum mesh (Nanjing Zhongjing Keyi). The precursor solution was then exposed to 405 nm light for 15 s to initiate crosslinking. Two groups of Silgels were prepared, the control group and the ethanol-treated group. Both groups were placed in 1.5 × SBF (Solarbio®) for mineralization. Samples were collected on days 0, 1, and 5. Samples from day 0 of both groups were not mineralized and were negatively stained with 0.2 % (wt/v) uranyl acetate for 30 s each. All samples were observed and analyzed using a field emission transmission electron microscope (JEOL F200) at 80 kV.

Mineralization of hydrogel disc samples: 30 % (wt/v) of SilMA gel-forming precursor solution was then filtered through a 0.22 μm Millex-GP filter and printed as 4 mm diameter, 1 mm high discs using a DLP 3D printer. The resulting Silgel discs were processed in two ways: the control group without any treatment and the ethanol-treated (24 h) group. Both groups were placed in 1.5 × SBF (Solarbio®) for mineralization. Samples were collected on days 0, 7, and 14. The harvested samples were sectioned and loaded with 300-mesh copper mesh (Nanjing Zhongjing Keyi). The middle areas of the slices were then observed and analyzed using a spherical differential correction projection electron microscope (FEI Titan G2 60–300) at 200 kV.

5.5. Rat subcutaneous mineralization assay

Two forms of Silgels were prepared and analyzed, the control group and the group treated with ethanol for 24 h. 30 % (wt/v) SilMA gel-forming precursor solution was filtered through a 0.22 μm Millex-GP filter, and then subjected to a 10 s irradiation with 405 nm light. The Silgels were prepared as cylinders (Diameter = 10 mm, Height = 5 mm) and then treated either as the control group or subjected to an ethanol treatment for 24 h followed by PBS treatment for 24 h (PBS treatment was to replace ethanol). The animals were anesthetized by using intraperitoneal injection with 40 mg/kg 1 % (wt/v) sodium pentobarbital of body weight. The skin on the dorsal region of the rat was prepared and disinfected with povidone-iodine in a sterile environment. Then 1-cm-long incision was made in the center of the back of the rat and the Silgel cylinders were implanted subcutaneously in rats. The incision was subsequently sutured. At week 4, the rats were sacrificed and samples were processed for subsequent analysis (3 biological replicates per group at each time point). Animal experiments were approved by Experimental Animal Welfare Ethics Committee of Zhejiang University (ZJU20200042).

5.6. SEM to characterize sections of samples after subcutaneous mineralization

For SEM analysis, the samples after sectioning were sprayed with gold and observed with a cold field emission scanning electron microscope (Hitachi SU8010).

5.7. Isolation of hBMSCs and adhesion efficiency of hBMSCs

Human bone marrow-derived stem cells (hBMSCs) were obtained from the femur of patients undergoing fracture operation with the approval of the Research Ethics Committee of the First Affiliated

Hospital, College of Medicine, Zhejiang University (ZJU2018392). hBMSCs were isolated by filtrating bone marrow through a 40 μm cell filter (Corning Inc, Corning, NY, USA). After filtering, the cells were centrifuged, resuspended and cultured in 95-mm dishes in L-DMEM complete growth medium. The cells were then cultured and passaged into new flasks. The Silgel discs were prepared as described above and treated in three ways, the first was the control group without treatment, the second was the ethanol treatment for 24 h followed by PBS treatment for 24 h (the purpose of PBS treatment was to replace the ethanol), and the third was the ethanol treatment for 24 h followed by PBS treatment for 24 h and mineralization in simulated body fluid for 4 weeks. The hBMSC suspensions (1 mL, 4×10^6 cells) were seeded on these groups of discs in 24-well culture plates and cultured with L-DMEM for 24 h. Then, the culture solution was replaced by L-DMEM containing AM/PI (Beyotime®) double-stained reagent and the discs were imaged under an upright two-photon fluorescence microscope (Olympus). Then, the discs were fixed with 2.5 % glutaraldehyde solution and 1.5 % osmium acid solution, followed by critical point drying and gold spraying. Finally, the morphology of Silgel discs and the cells were observed by scanning electron microscopy (Hitachi SU8010).

5.8. Expression detection of alkaline phosphatase (ALP)

The expression level of alkaline phosphatase (ALP) was utilized to represent the osteogenic differentiation efficiency of hBMSCs. The procedure involved the preparation of the Silgel discs described above. The discs were treated in three ways, the first was the Control group without treatment, the second was the ethanol treatment for 24 h followed by PBS treatment for 24 h (the purpose of PBS treatment was to replace the ethanol), and the third was the ethanol treatment for 24 h followed by PBS treatment for 24 h and mineralization in 1.5 × SBF for 4 weeks. The hBMSC suspensions (1 mL; 4×10^6 cells) were seeded on these groups of discs in 24-well culture plates and cultured with L-DMEM for 24 h, followed by osteogenic induction medium culturing for 7 days, with changing the medium every other day. After 7 days of osteogenic induction culture, samples from each group were fixed with 4 % formaldehyde solution, followed by staining with BCIP/NBT alkaline phosphatase color development kit (C3206, Beyotime®) and being observed with light microscopy (Olympus). For other replicates, cells were lysed with cell lysis solution, and the lysate was subjected to substrate color development reaction according to the protocol of the alkaline phosphatase assay kit (P0321 M, Beyotime®). The absorbance at 415 nm was detected with a multifunctional microplate system (Molecular Devices), and enzyme activity was calculated.

5.9. Alizarin Red S (ARS) staining

The procedure involved the preparation of the Silgel discs, hBMSCs seeding and osteogenic differentiation as described above. After 21 days of osteogenic differentiation, the samples were fixed and stained using an ARS staining kit for osteogenesis (Beyotime®). After that, the samples were observed using a microscope and quantitatively analyzed by recording the OD absorbance at 405 nm respectively.

5.10. Quantitative real-time PCR (qPCR) analysis

qPCR was also utilized to evaluate the osteogenic differentiation efficiency of hBMSCs. The hBMSCs suspensions (2 mL; 4×10^6 cells) were seeded on Silgel samples in 24-well culture plates and cultured with L-DMEM (Gibco®) for 24 h, followed by osteogenic induction medium culturing for 7 days, with changing the medium every other day. Trizol (9109, Takara®) was used to extract the total RNA and the RNA was reverse-transcribed to cDNA using RT master mix (Vazyme, China). qPCR was performed using SYBR Mix (Vazyme, China). The primers of Gapdh, OCN, ALP, COL-1, and RUNX2 are listed in Table 1. Values were calculated with the $2^{-\triangle\triangle Ct}$ method and normalized to the Gapdh expression.

Table 1
Primers of tested human genes.

Gene	Forward Sequence (5′-3′)	Reverse sequence (5′-3′)
Gapdh	TGACGCTGGGGCTGGCATTG	GGCTGGTGGTCCAGGGGTCT
OCN	TCTCCAGGCACCCTTCTTTCC	ACAGGCCCACAGATTCCTCTTC
ALP	AGCCCTTCACTGCCATCCTGT	GACTGCGCCTGGTAGTTGTTGT
COL-1	CGATGGATTCCAGTTCGAGTAT	CATCGACAGTGACGCTGTAGG
RUNX2	GTGATAAATTCAGAAGGGAGG	CTTTTGCTAATGCTTCGTGT

5.11. DLP 3D printing

The 30 % (wt/v) SilMA ink was prepared, which also contained 1 % (wt/v) LAP as initiator. A model of the bone scaffold with haversian-mimicking structure was designed by CAD software and was saved as a stereolithographic (STL) file. Then, the STL file was sliced along the Z direction (50 μm for each layer) to generate the JOB file to be printed. The model was a cylinder with a height of 6 mm and a diameter of 8 mm, in which there were seven cylindrical canals with a diameter of 2 mm parallel to the height of the cylinder and four perpendicular to the height of the cylinder, interpenetrating each other. Then the 30 % (wt/v) SilMA ink was added to the ink container for printing (the light intensity: 30mW/cm2; exposure time: 1500 ms for each layer). The scaffolds were gently scraped off with a cell spatula after printing, and then the uncross-linked SilMA ink was briefly rinsed with PBS. The printed scaffolds were divided into three groups, the first group was the untreated Silgel scaffold (SGS); the second group was the ethanol-treated Silgel scaffold (ES), treated with ethanol for 24 h; and the third group was treated with ethanol for 24 h, followed by immersion in 1.5 × SBF mineralized for 4 weeks (Ethanol-treated and mineralized Silgel scaffold, EMS).

5.12. SEM to characterize sections of scaffolds

Three forms of Silgels scaffold, SGS, ES and EMS, were prepared and embedded with Optimal cutting temperature compound (OCT, Sakura Tissue-Tek®). Then, the samples were performed in frozen sections with a thickness of 100 μm. The sections were firstly washed in dH_2O, then placed at −80 °C overnight, followed by freeze-drying and gold spraying. Finally, the sections were observed with a cold field emission scanning electron microscope (Hitachi SU8010) and analyzed by energy dispersive X-ray spectroscopy (EDS).

5.13. Compression test

The compressive stress-strain measurements were performed using an electromechanical test system (MTS Criterion Model 41) with a 1 kN sensor. Three forms of Silgel scaffolds, including SGS, ES and EMS were prepared as described above. The compressive strain rate was 5 mm/min and the strain level was set to 90 % of the original height. The compression modulus was calculated as the slope of the stress-strain curves in the strain between 10 % and 20 %.

5.14. Bone defect repair experiments

For *in situ* repair of bone defects in rabbits, male New Zealand rabbits were chosen and randomized into four groups: Blank defeats, SGS, ES, EMS and autologous cancellous bone (ACB). In brief, the rabbits were anesthetized with Pentobarbital (3 % (wt/v), 1 mL/kg) by intravenous injection at the ear margin, followed by skin preparation of the leg in a sterile environment and disinfection with povidone-iodine. A cylindrical defeat was created by using a bone drill at the femoral epicondyle of the knee joint, with a height of 6 mm and a diameter of 8 mm. Then, scaffolds were implanted (blank defect without implantation). The incision

was sutured and the rabbits were given intramuscular injections of penicillin potassium for three consecutive days. After 1 week, the rabbits were sacrificed and tissues at the defect were collected for transcriptome sequencing. At 4 weeks, the rabbits were sacrificed. Then the distal femur (at the molded site) was removed with bone forceps and prepared for subsequent analysis. Animal experiments were approved by the Experimental Animal Welfare Ethics Committee of Zhejiang University (ZJU20220324).

5.15. Micro-CT imaging and analysis

A small animal live tomography imaging system (Milabs, U-CT-XUHR) was applied for micro-CT imaging and analysis of the femur samples. A cylindrical region of the same size as the modeling area (8 mm in diameter, 6 mm in depth) was defined to analyze the bone regeneration status within the defect site, with the threshold set to 400 for soft tissue and 1600 for bone tissue. After 3D reconstruction, the bone tissue volume/total tissue volume (BV/TV) and other data were automatically determined.

5.16. Histological evaluation

The femur samples were fixed with 4 % paraformaldehyde for 1 week and then washed with a constant flow of tap water overnight to remove residual paraformaldehyde. Then, the samples were decalcified in Ethylenediaminetetraacetic acid (EDTA) solution for 2 months. The samples were then washed with tap water overnight and then dehydrated by graded ethanol (50%–100 %). After that, samples were cleared in xylene and embedded in paraffin. The embedded paraffin blocks were sliced using a paraffin microtome with a section thickness of 7 μm. The slices were classically stained with hematoxylin and eosin (HE) and Masson's trichrome (MT) kits (Solarbio®).

5.17. Transcriptome sequencing

The transcriptomes of all samples were paired-end sequenced at the Beijing Genomics Institute (BGI Shenzhen)on a MGISEQ-2000 platform. After 7 days of implantation, the rabbits were sacrificed. Then the distal femur (at the molded site) was removed with bone forceps and put into liquid nitrogen for quick freezing. The samples were stored at −80 °C and transferred to UW Genetics for DNBSEQ eukaryotic strand-specific transcriptome library construction and sequencing. RNA was extracted from samples. Then qualified total RNA samples were digested with DNase I and enriched for mRNA using Oligo (dT) magnetic beads. Processed by reverse transcription and PCR, cDNA libraries were prepared according to the manufacturer's protocol. The data obtained from sequencing were called raw reads or raw data, and the raw reads were subsequently subjected to quality control (QC) to determine if the sequencing data were suitable for subsequent analysis. After QC, the filtered clean reads were compared to the reference sequence. The comparison determined whether the comparison results passed the second QC by counting the comparison rate and the distribution of reads on the reference sequence. For passed clean reads, quantitative gene analysis, various analyses based on gene expression levels (principal component, correlation, differential gene screening, etc.) and deeper mining analysis such as Gene Ontology (GO) functional significance enrichment analysis, pathway significance enrichment analysis, clustering and reciprocal network were performed for the differentially expressed genes between the screened samples.

5.18. Statistical analysis

The sample size of the data for statistical analysis was at least 3, and all quantitative data were presented as mean ± standard deviation. One-way analysis of variance (ANOVA) was performed to assess whether statistical differences existed between groups. The significance level was presented as $^{*}P < 0.05$, $^{**}P < 0.01$, $^{***}P < 0.001$, and $^{****}P < 0.0001$.

Funding

This work was supported by the National Key Research and Development Program of China (2023YFB3813000), and the National Natural Science Foundation of China (T2121004, 92268203, 32371411).

Ethics approval and consent to participate

1. Human bone marrow-derived mesenchymal stem cells (hBMSCs), extracted from bone marrow of patients with femoral fracture, informed consent was obtained. The experiment was approved by the Ethics Committee of the First Affiliated Hospital of Zhejiang University School of Medicine (Ethics batch number: ZJU2018392).

2. Sprague-Dawley (SD) rat, male, weighing about 250 g, purchased from Experimental Animal Center of Zhejiang University. Animal experiments were approved by Experimental Animal Welfare Ethics Committee of Zhejiang University (Ethics batch number: ZJU20200042); New Zealand white rabbit, male, about 3 kg, purchased from the Experimental Animal Center of Zhejiang University. Animal experiments were approved by the Experimental Animal Welfare Ethics Committee of Zhejiang University (Ethics batch number: ZJU20220324).

CRediT authorship contribution statement

Renjie Liang: Writing – original draft, Validation, Software, Project administration, Methodology, Investigation, Formal analysis, Data curation, Conceptualization. **Rui Li:** Writing – original draft, Validation, Methodology, Investigation, Data curation. **Weidong Mo:** Writing – original draft, Validation, Methodology, Investigation. **Xianzhu Zhang:** Writing-original article, Validation, Investigation. **Jinchun Ye:** Investigation. **Chang Xie:** Investigation. **Wenyue Li:** Investigation. **Zhi Peng:** Investigation, Data curation. **Yuqing Gu:** Investigation. **Yuxuan Huang:** Investigation. **Shufang Zhang:** Resources, Data curation. **Xiaozhao Wang:** Writing – review & editing, Supervision, Data curation. **Hongwei Ouyang:** Writing – review & editing, Supervision, Resources, Funding acquisition, Conceptualization.

Declaration of competing interest

The authors declare that they have no known competing financial interests or personal relationships that could have appeared to influence the work reported in this paper.

Appendix A. Supplementary data

Supplementary data to this article can be found online at https://doi.org/10.1016/j.bioactmat.2024.06.024.

References

[1] T.A. DeCoster, R.J. Gehlert, E.A. Mikola, M.A. Pirela-Cruz, Management of posttraumatic segmental bone defects, J. Am. Acad. Orthop. Surg. 12 (1) (2004) 28–38.
[2] C. Mauffrey, B.T. Barlow, W. Smith, Management of segmental bone defects, J. Am. Acad. Orthop. Surg. 23 (3) (2015) 143–153.
[3] G.L. Koons, M. Diba, A.G. Mikos, Materials design for bone-tissue engineering, Nat. Rev. Mater. 5 (8) (2020) 584–603.
[4] R. Dimitriou, E. Jones, D. McGonagle, P.V. Giannoudis, Bone regeneration: current concepts and future directions, BMC Med. 9 (2011) 66.
[5] A.L. Overmann, C. Aparicio, J.T. Richards, I. Mutreja, N.G. Fischer, S.M. Wade, B. K. Potter, T.A. Davis, J.E. Bechtold, J.A. Forsberg, D. Dey, Orthopaedic osseointegration: implantology and future directions, J. Orthop. Res. 38 (7) (2020) 1445–1454, *official publication of the Orthopaedic Research Society*.
[6] P. Dec, A. Modrzejewski, A. Pawlik, Existing and novel biomaterials for bone tissue engineering, Int. J. Mol. Sci. 24 (1) (2022).

[7] Y. Abu-Amer, I. Darwech, J.C. Clohisy, Aseptic loosening of total joint replacements: mechanisms underlying osteolysis and potential therapies, Arthritis Res. Ther. 9 (2007).

[8] Z. Ji, Y. Wan, H. Wang, M. Yu, Z. Zhao, T. Wang, G. Ma, S. Fan, Z. Liu, Effects of surface morphology and composition of titanium implants on osteogenesis and inflammatory responses: a review, Biomed. Mater. 18 (4) (2023).

[9] E. Marukawa, M. Tamai, Y. Takahashi, I. Hatakeyama, M. Sato, Y. Higuchi, H. Kakidachi, H. Taniguchi, T. Sakamoto, J. Honda, K. Omura, H. Harada, Comparison of magnesium alloys and poly-l-lactide screws as degradable implants in a canine fracture model, J. Biomed. Mater. Res. B Appl. Biomater. 104 (7) (2016) 1282–1289.

[10] Z. Li, T. Du, C. Ruan, X. Niu, Bioinspired mineralized collagen scaffolds for bone tissue engineering, Bioact. Mater. 6 (5) (2021) 1491–1511.

[11] G.A. Rico-Llanos, S. Borrego-Gonzalez, M. Moncayo-Donoso, J. Becerra, R. Visser, Collagen type I biomaterials as scaffolds for bone tissue engineering, Polymers 13 (4) (2021).

[12] S. Yao, X. Lin, Y. Xu, Y. Chen, P. Qiu, C. Shao, B. Jin, Z. Mu, N. Sommerdijk, R. Tang, Osteoporotic bone recovery by a highly bone-inductive calcium phosphate polymer-induced liquid-precursor, Adv. Sci. 6 (19) (2019) 1900683.

[13] K. Lin, D. Zhang, M.H. Macedo, W. Cui, B. Sarmento, G. Shen, Advanced collagen-based biomaterials for regenerative biomedicine, Adv. Funct. Mater. 29 (3) (2019).

[14] F. Gao, Z. Xu, Q. Liang, B. Liu, H. Li, Y. Wu, Y. Zhang, Z. Lin, M. Wu, C. Ruan, W. Liu, Direct 3D printing of high strength biohybrid gradient hydrogel scaffolds for efficient repair of osteochondral defect, Adv. Funct. Mater. 28 (13) (2018).

[15] M.A. Heinrich, W. Liu, A. Jimenez, J. Yang, A. Akpek, X. Liu, Q. Pi, X. Mu, N. Hu, R. M. Schiffelers, J. Prakash, J. Xie, Y.S. Zhang, 3D bioprinting: from benches to translational applications, Small 15 (23) (2019) e1805510.

[16] B. Kundu, R. Rajkhowa, S.C. Kundu, X. Wang, Silk fibroin biomaterials for tissue regenerations, Adv. Drug Deliv. Rev. 65 (4) (2013) 457–470.

[17] W. Zhang, L. Chen, J. Chen, L. Wang, X. Gui, J. Ran, G. Xu, H. Zhao, M. Zeng, J. Ji, L. Qian, J. Zhou, H. Ouyang, X. Zou, Silk fibroin biomaterial shows safe and effective wound healing in animal models and a randomized controlled clinical trial, Adv. Healthcare Mater. 6 (10) (2017).

[18] S.H. Kim, Y.K. Yeon, J.M. Lee, J.R. Chao, Y.J. Lee, Y.B. Seo, M.T. Sultan, O.J. Lee, J. S. Lee, S.-i. Yoon, I.-S. Hong, G. Khang, S.J. Lee, J.J. Yoo, C.H. Park, Precisely printable and biocompatible silk fibroin bioink for digital light processing 3D printing, Nat. Commun. 9 (2018).

[19] W.H. Elliott, W. Bonani, D. Maniglio, A. Motta, W. Tan, C. Migliaresi, Silk hydrogels of tunable structure and viscoelastic properties using different chronological orders of genipin and physical cross-linking, ACS Appl. Mater. Interfaces 7 (22) (2015) 12099–12108.

[20] C. Guo, C. Li, H.V. Vu, P. Hanna, A. Lechtig, Y. Qiu, X. Mu, S. Ling, A. Nazarian, S. J. Lin, D.L. Kaplan, Thermoplastic moulding of regenerated silk, Nat. Mater. 19 (1) (2020) 102–110.

[21] T. Shu, Z. Lv, C.-T. Chen, G.X. Gu, J. Ren, L. Cao, Y. Pei, S. Ling, D.L. Kaplan, Mechanical training-driven structural remodeling: a rational route for outstanding highly hydrated silk materials, Small 17 (33) (2021).

[22] K. Numata, S. Yamazaki, T. Katashima, J.A. Chuah, N. Naga, T. Sakai, Silk-pectin hydrogel with superior mechanical properties, biodegradability, and biocompatibility, Macromol. Biosci. 14 (6) (2014) 799–806.

[23] A. Takeuchi, C. Ohtsuki, M. Kamitakahara, S. Ogata, T. Miyazaki, M. Tanihara, Biomimetic deposition of hydroxyapatite on a synthetic polypeptide with beta sheet structure in a solution mimicking body fluid, J. Mater. Sci. Mater. Med. 19 (1) (2008) 387–393.

[24] Y. Huang, Z.Y. Zou, H. Ping, L.W. Lei, J.J. Xie, H. Xie, Z.Y. Fu, Mineralization of calcium phosphate induced by a silk fibroin film under different biological conditions, RSC Adv. 11 (30) (2021) 18590–18596.

[25] R. Kino, T. Ikoma, A. Monkawa, S. Yunoki, M. Munekata, J. Tanaka, T. Asakura, Deposition of bone-like apatite on modified silk fibroin films from simulated body fluid, J. Appl. Polym. Sci. 99 (5) (2006) 2822–2830.

[26] L. Nie, H. Zhang, A.S. Ren, Y.Z. Li, G. Fu, R.D. Cannon, P. Ji, X.H. Wu, S. Yang, Nano-hydroxyapatite mineralized silk fibroin porous scaffold for tooth extraction site preservation, Dent. Mater. 35 (10) (2019) 1397–1407.

[27] J.H. He, G.B. Chen, M.Y. Liu, Z.L. Xu, H. Chen, L. Yang, Y.G. Lv, Scaffold strategies for modulating immune microenvironment during bone regeneration, Mater. Sci. Eng., C 108 (2020).

[28] Y. Zhang, R. Sheng, J. Chen, H. Wang, Y. Zhu, Z. Cao, X. Zhao, Z. Wang, C. Liu, Z. Chen, P. Zhang, B. Kuang, H. Zheng, C. Shen, Q. Yao, W. Zhang, Silk fibroin and sericin differentially potentiate the paracrine and regenerative functions of stem cells through multiomics analysis, Adv. Mater. 35 (20) (2023).

[29] R. Liang, X. Shen, C. Xie, Y. Gu, J. Li, H. Wu, Y. Wen, B. Wu, K. Zhao, Y. Wu, X. Yao, S. Zhang, Y. Hong, H. Ouyang, Silk gel recruits specific cell populations for scarless skin regeneration, Appl. Mater. Today 23 (2021).

[30] P. Guo, X. Liu, P. Zhang, Z. He, Z. Li, M. Alini, R.G. Richards, S. Grad, M. J. Stoddart, G. Zhou, X. Zou, D. Chan, W. Tian, D. Chen, M. Gao, Z. Zhou, S. Liu, A single-cell transcriptome of mesenchymal stromal cells to fabricate bioactive hydroxyapatite materials for bone regeneration, Bioact. Mater. 9 (2022) 281–298.

[31] T. Zhang, H. Zhang, L. Zhang, S. Jia, J. Liu, Z. Xiong, W. Sun, Biomimetic design and fabrication of multilayered osteochondral scaffolds by low-temperature deposition manufacturing and thermal-induced phase-separation techniques, Biofabrication 9 (2) (2017).

[32] C.M. Schoenfeld, E.P. Lautenschlager, P.R. Meyer Jr., Mechanical properties of human cancellous bone in the femoral head, Med. Biol. Eng. 12 (3) (1974) 313–317.

[33] B. Marelli, C.E. Ghezzi, A. Alessandrino, J.E. Barralet, G. Freddi, S.N. Nazhat, Silk fibroin derived polypeptide-induced biomineralization of collagen, Biomaterials 33 (1) (2012) 102–108.

[34] X. Fu, G. Liu, A. Halim, Y. Ju, Q. Luo, A.G. Song, Mesenchymal stem cell migration and tissue repair, Cells 8 (8) (2019).

[35] N.J. Panetta, D.M. Gupta, M.T. Longaker, Bone regeneration and repair, Curr. Stem Cell Res. Ther. 5 (2) (2010) 122–128.

[36] L. Shang, J. Shao, S. Ge, Immunomodulatory properties: the accelerant of hydroxyapatite-based materials for bone regeneration, Tissue Eng. C Methods 28 (8) (2022) 377–392.

[37] Y. Xiong, B.B. Mi, Z. Lin, Y.Q. Hu, L. Yu, K.K. Zha, A.C. Panayi, T. Yu, L. Chen, Z. P. Liu, A. Patel, Q. Feng, S.H. Zhou, G.H. Liu, The role of the immune microenvironment in bone, cartilage, and soft tissue regeneration: from mechanism to therapeutic opportunity, Military. Med. Res. 9 (1) (2022) 65.

[38] Z. Peng, C. Xie, S.C. Jin, J.J. Hu, X.D. Yao, J.C. Ye, X.Z. Zhang, J.X. Lim, B.B. Wu, H.Y. Wu, R.J. Liang, Y. Wen, J.H. Huang, X.H. Zou, H.W. Ouyang, Biomaterial based implants caused remote liver fatty deposition through activated blood-derived macrophages, Biomaterials 301 (2023).

[39] J.C. Doloff, O. Veiseh, R. de Mezerville, M. Sforza, T.A. Perry, J. Haupt, M. Jamiel, C. Chambers, A. Nash, S. Aghlara-Fotovat, J.L. Stelzel, S.J. Bauer, S.Y. Neshat, J. Hancock, N.A. Romero, Y.E. Hidalgo, I.M. Leiva, A.M. Munhoz, A. Bayat, B. M. Kinney, H.C. Hodges, R.N. Miranda, M.W. Clemens, R. Langer, The surface topography of silicone breast implants mediates the foreign body response in mice, rabbits and humans, Nat. Biomed. Eng. 5 (10) (2021) 1115–1130.

[40] P.X. Chen, L.H. Li, L.L. Dong, S.X. Wang, Z. Huang, Y.N. Qan, C.L. Wang, W.Q. Liu, L. Yang, Gradient biomineralized silk fibroin nanofibrous scaffold with osteochondral inductivity for integration of tendon to bone, ACS Biomater. Sci. Eng. 7 (3) (2021) 841–851.

[41] B.W.M. de Wildt, R. van der Meijden, P.A.A. Bartels, N. Sommerdijk, A. Akiva, K. Ito, S. Hofmann, Bioinspired silk fibroin mineralization for advanced in vitro bone remodeling models, Adv. Funct. Mater. 32 (41) (2022).

[42] P. Gupta, M. Adhikary, M.J. Christakiran, M. Kumar, N. Bhardwaj, B.B. Mandal, Biomimetic, osteoconductive non-mulberry silk fiber reinforced tricomposite scaffolds for bone tissue engineering, ACS Appl. Mater. Interfaces 8 (45) (2016) 30797–30810.

[43] H.J. Kim, U.J. Kim, H.S. Kim, C.M. Li, M. Wada, G.G. Leisk, D.L. Kaplan, Bone tissue engineering with premineralized silk scaffolds, Bone 42 (6) (2008) 1226–1234.